JOURNAL OF AEROSPACE INFORMATION SYSTEMS
Vol. 13, No. 4, April 2016

Unmanned Aircraft System Navigation in the Urban Environment: A Systems Analysis

Justin R. Rufa* and Ella M. Atkins†
University of Michigan, Ann Arbor, Michigan 48109

DOI: 10.2514/1.I010280

Unmanned aircraft system navigation in urban environments requires consideration of which combination of sensors can provide the most accurate navigation results in a dynamically changing environment. The traditional Global Positioning System, although useful in open spaces, degrades severely when in urban canyons requiring other complementary sensors to provide position and velocity measurements when necessary. One well-known solution is vision-based sensors that provide measurements through optical flow. Another possibility is the long-term evolution network that is currently used for cellular voice and data transmission as well, as coarse Global-Positioning-System-independent navigation. This paper reviews sensor accuracy and availability as a function of environment characteristics. A simulation framework integrates these different types of sensors to allow for efficient high-level testing of sensor combinations and fusion algorithms. Results show that long-term evolution slightly improves position accuracy unless another exteroceptive position sensor such as vision is available. Sinusoidal trajectories that rise above the urban environment also show increases in accuracy as Global Positioning System navigation becomes available during these short windows.

Nomenclature

A	=	state transition Jacobian matrix
B	=	control input Jacobian matrix
dt	=	simulation time step, s
F_T	=	unmanned aircraft system propeller thrust, N
H	=	measurement sensitivity Jacobian matrix
h	=	unmanned aircraft system altitude above ground level, m
K	=	Kalman gain matrix
$\bar{K}$	=	linear quadratic regulator controller gain matrix
N_p, N_{eff}	=	number of particles and number of effective particles
P	=	estimated covariance matrix
p, q, r	=	unmanned aircraft system body-fixed roll rate, pitch rate, and yaw rate, rad/s
Q	=	process noise covariance matrix
$\bar{Q}$	=	linear quadratic regulator state weighting matrix
$\tilde{q}$	=	number of sensors providing measurement
R	=	measurement noise covariance matrix
$\bar{R}$	=	linear quadratic regulator control input weighting matrix
S	=	Kalman filter residual covariance matrix
$\boldsymbol{u}$	=	control input vector
V_T	=	unmanned aircraft system airspeed, m/s
$\boldsymbol{v}$	=	measurement noise vector
$\boldsymbol{w}$	=	process noise vector
$\boldsymbol{X}$	=	particle set
$\boldsymbol{x}$, $\hat{\boldsymbol{x}}$	=	true state vector and estimated state vector
x_N	=	unmanned aircraft system longitudinal position, m
x_N, x_E, h	=	unmanned aircraft system longitudinal position, lateral position, and altitude, m
$\boldsymbol{x}^i$	=	particle vector
$\boldsymbol{z}$	=	measurement vector
α, β	=	unmanned aircraft system angle of attack and angle of sideslip, rad
δa, δe, δr	=	unmanned aircraft system aileron deflection, elevator deflection, and rudder deflection, % deflection
ν	=	Kalman filter residual vector
$\bar{\rho}$	=	linear quadratic regulator tuning parameter
ϕ, θ, ψ	=	unmanned aircraft system roll angle, pitch angle, and yaw angle, rad

I. Introduction

AS TECHNOLOGY matures, small unmanned aircraft systems (UAS) can begin conducting urban missions such as law enforcement, antiterrorism, riot control, traffic surveillance, natural disaster monitoring, emergency medical/flood delivery, agriculture, and communication relay [1]. The biggest challenge is to navigate safely while avoiding the many obstacles in the urban environment, including

Received 29 April 2014; revision received 17 July 2015; accepted for publication 24 August 2015; published online XX epubMonth XXXX.

*Ph.D. Candidate, Department of Aerospace Engineering, 1320 Beal Ave. Student Member AIAA.
†Associate Professor, Department of Aerospace Engineering, 1320 Beal Ave. Associate Fellow AIAA.

buildings, overpasses, sky bridges, antennas, etc. In 2007, a study in the United Kingdom concluded that sensor obscuration would be an impediment to enabling safe UAS operations for missions such as urban law enforcement, showing the need for navigation and control systems independent of any one data source [2]. Global Positioning System (GPS) degradation, whether due to natural phenomena or manmade structures [3], is also problematic, due to increased geometric dilution of precision [4]. In 2003, the effects of the urban environment on GPS availability and error were quantified in a study in the Wan Chai district of Hong Kong [5]. GPS denial must also be considered, especially given an example such as the inadvertent Newark Airport GPS outage event from November 2009 through April 2010 [6]. To address this problem, both the Defense Advanced Research Projects Agency [7] and BAE Systems [8] examined signals of opportunity, including cellular network, television, wireless fidelity (known as Wi-Fi), and even signals emanating from other satellites to determine if any would be viable for GPS-independent navigation. Although local signals from onboard sensors such as cameras and light detection and ranging (LIDAR) allow mapping the local environment, Wi-Fi and cellular network protocols such as long-term evolution (LTE) also might support inertial navigation, particularly in GPS-denied urban environments.

This paper investigates urban navigation for unmanned aircraft systems using a system simulation package developed for this purpose. The simulation is built on generalized data objects that provide modularity and facilitate customization of air vehicle performance, sensor availability and noise, estimation filter types and tunings, and urban environment characteristics. This structure facilitates trade studies of navigation performance for different aircraft as a function of environments and available sensor suites. Specific innovations include the introduction of the time-delayed LTE measurement as a measurement source, the use of environment-dependent GPS and LTE availability and accuracy values, and fusion of any combination of navigation signals in the propagated state estimate. This paper also provides a concise summary of UAS sensor measurement noise values over a variety of literature sources that can serve as a standalone reference for future research efforts.

This remainder of this paper is divided into background, simulation development, simulation execution, results, and conclusions/future work. The background section discusses previous urban canyon navigation research, sensor measurement specifics including expected availability and accuracy, and the proposed solution. The Simulation Development section (Sec. III) details the software framework; guidance, navigation, and control modules; state estimation filters; and the proposed sensor fusion strategy. The Simulation Execution section (Sec. IV) discusses the specific simulation parameters. The Results section (Sec. V) presents navigation accuracy findings from multiple urban environments, examining the effects of delay GPS, LTE, and vision system delay as needed. The final section (Sec. VI) provides a summary of major conclusions and proposes areas for further investigation.

II. Background

A. Previous Urban Navigation Work

Since the early 1990s, researchers have studied urban canyon vehicle navigation in the presence of degraded and sometimes unavailable GPS sensor data. This research has motivated solutions ranging from GPS only to multisensor fusion using additional sources such as inertial sensors [9–14], a priori urban maps [15–19], and ground-based navigation transmitters [20–22]. The large variety of contrasting stimuli and static objects in the urban environment make vision and laser solutions appealing alternatives to GPS. Several works have studied the accuracy of vision-based UAS navigation using either optic flow methods [23–26] or feature detection/localization based on environmental features [27–30]. With rigid structures in the environment, lasers have also proven useful for urban navigation, giving submeter accuracy in ground applications [31,32]. Vision and laser solutions can even be used together, exploiting the benefits of the laser when in close proximity to surfaces and deferring to vision when further from structures or terrain [33].

B. UAS Sensors

1. *Inertial Measurement Unit*

The inertial measurement unit (IMU) for a small UAS uses generally consists of three-axis gyroscopes, three-axis accelerometers, and a three-axis magnetometer to provide measurements of the aircraft's angular velocities as well as gravity and magnetic north vectors. These raw measurements are postprocessed and filtered to convert data into roll, pitch, yaw, and angular rate information accounting for any noise and bias in the data due to environmental conditions [34]. Some of the filters used to accomplish this include a complementary filter [34,35], an extended Kalman filter (EKF) [36], and an unscented Kalman filter [37].

Since this research is focused on postprocessed attitude and heading reference system (AHRS)-type sensor outputs, the measurement models for body-fixed angular rates and Euler attitude angles will add zero mean white Gaussian noise to the true values of the state. Typical angular rate 1σ noise values are generally close to 0.5 deg/s [38–40]. Euler angle 1σ noise values are generally similar for pitch and roll in the range of 0.6–3 deg [34,37,41]. The main advantage of this sensor is that its measurements are based on inertial accelerations, which are not affected by urban buildup. However, the main disadvantage is that the sensor data integration to approximate position and attitude suffers drift over time.

2. *GPS/IMU*

In navigation applications, an important part of the GPS receiver position calculation is determining the slowly time-varying position error. This error can be calculated for 1σ root-mean-square (RMS) error as the product of the dilution of precision and the filtered user range equivalent error (UERE) in the horizontal and vertical directions independently. The horizontal dilution of precision and vertical dilution of precision are approximately 1.3 and 1.8, respectively, with the UERE ranging from 4 to 5.1 m when taking into account factors such as clock error, atmosphere, multipath, receiver, and ephemeris [42,43]. Using this model, the GPS 1σ position error in both horizontal dimensions is roughly 3.67 m, and it is roughly 7.2 m in the vertical direction.

When GPS measurements are combined with inertial measurements in a navigation filter, the UAS position, velocity, and attitude can be estimated accurately. Nemra and Aouf [44] used a loosely coupled GPS/inertial navigation system (INS) with a state-dependent Riccati equation filter to yield position errors between 1 and 3 m. Rhudy et al. [45] also used a loosely coupled system with multiple GPS antennas and an unscented Kalman filter to yield roll and pitch errors between 0.8 deg and roughly 1.5 deg using different techniques to filter the GPS and INS measurements.

When in the urban environment, GPS degradation is common due to factors such as multipath, masking, or even intentional acts such as jamming or spoofing. Past research has shown GPS availability rates in this type of environment range from 30 to 50% [5,10,13]. To quantify GPS accuracy in the urban environment, Lu et al. [5] conducted GPS accuracy trials in the Wan Chai area of Hong Kong (seen in Fig. 1), which is known to have one of the densest high-rise building cores on the island. When a GPS solution was available, the accuracy was worse than 20 m for 40% of the points and worse than 100 m for 9% of the points.

In a less dense but large urban environment, MacGougan et al. [46] conducted a driving trial in Vancouver, British Columbia, Canada, as seen in Fig. 2. They found that the two-dimensional root-mean-square position error ranged from 10.8 to 23.1 m, with the RMS horizontal dilution of

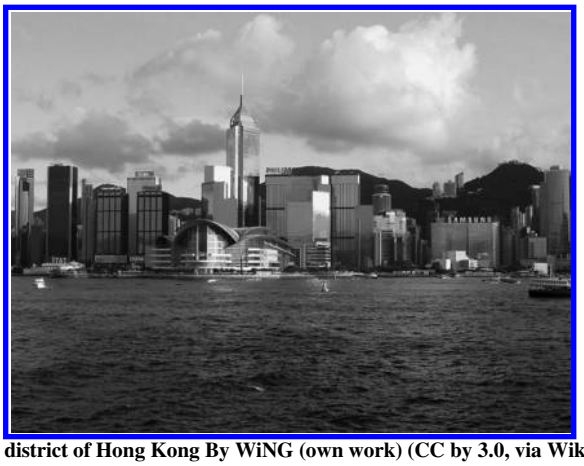

Fig. 1 Wan Chai district of Hong Kong By WiNG (own work) (CC by 3.0, via Wikimedia Common).

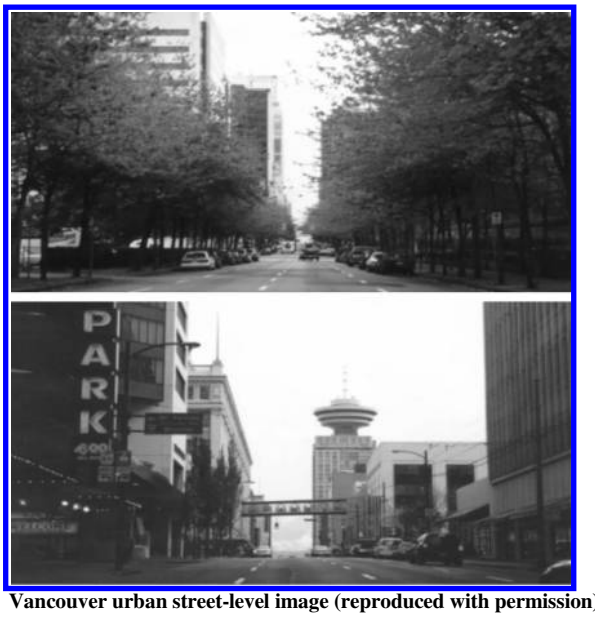

Fig. 2 Vancouver urban street-level image (reproduced with permission) [46].

precision ranging from 4.0 to 7.0. The RMS error for height ranged from 11.9 to 62.4 m. During a walking trial of Görlitz, Modsching et al. [47] found that the mean two-dimensional error was 2.42 m in the case of less urban buildup (Fig. 3a) and 15.43 m with more urban buildup (Fig. 3b).

3. Vision

An area of active research in UAS urban navigation is the use of computer vision to provide navigation information to a filter, generating position, airspeed, and attitude estimates. One of the largest advantages of using this type of sensor is that it does not depend on any type of manmade electromagnetic transmission to work properly, making it a complementary sensor to GPS. However, these sensors are only effective when in properly lighted high-contrast environments. These sensors use a variety of different techniques broadly described as optical flow or feature detection/localization.

a. Optical Flow. Optical flow is defined in [48] as the distribution of apparent velocities of brightness pattern movements in an image. It is generally calculated by comparing pixels in sequential images to determine the local velocity of the camera that is capturing the images. This concept can be applied to a UAS operating in an urban canyon by attaching a camera to the vehicle and calculating the apparent local velocities of adjacent buildings or the street below.

An ideal optical flow application to the urban environment is the "centering response," with biological inspiration from bees. Reference [49] explains that bees are able to hold this centerline trajectory by equalizing the apparent motion images on their retinas. This phenomenon has been demonstrated on UAS operating in urban canyons, both in simulations [23,50] and in experiments [51,52]. In addition to maintaining a centerline trajectory, further simulation and experiments have shown that vehicles equipped with combined optical flow-stereo sensors can also navigate 90 deg turns in a simulated urban canyon [25].

b. Feature Detection/Localization. One application of feature detection/localization uses vanishing points to measure both aircraft pitch and roll angles [29]. Once these vanishing points are calculated at any time step in which they are available from the image (updated at 5 Hz), they can be used in an EKF to reset the error in the IMU-based attitude angle estimate (updated at 100 Hz). Hwangbo and Kanade [29] demonstrated this technique with simulation-based pitch and roll 1σ error in the range of 1.5–2.25 deg and flight-test-based pitch and roll 1σ errors between 0.85 and 2.5 deg.

Fig. 3 Gorlitz urban buildup images (reproduced with permission) [47].

4. Air Data System

In addition to the AHRS, another existing small UAS sensor is the air data system (ADS) [53]. Most ADSs include, at minimum, a static pressure port to generate altitude measurements and a dynamic pressure port, which along with the static port generates airspeed measurements. Others include multiple dynamic pressure and static pressure measurement locations to generate angle of attack α and angle of sideslip β values [54,55]. Typical 1σ altitude accuracy ranges from 1.5 to 3 m [56,57]. Airspeed 1σ accuracy is between 1 and 1.5 m/s [54,57]. Angle-of-attack and angle-of-sideslip 1σ accuracy, using a differential pressure probe, are roughly 1 deg. The main advantage of an air data system is that it provides pressure-based measurements independent of all other sensors. However, in an urban environment with the potential for quickly shifting winds and gusts, airspeed measurements could change quickly and drastically, and they may not always be reliable.

5. Long-Term Evolution

The long-term evolution cellular network provides another preexisting signal that might increase navigation accuracy [58]. Due to the Federal Communications Commission's enhanced 911 location accuracy requirements, devices must already meet network-calculated accuracy of at least 300 m for 90% of the requested position fixes [59]. Although cellular carriers do not typically publish the accuracy of their geolocation techniques (because these are considered proprietary), they may be as accurate as 3 to 31 m [60,61].

Figure 4 shows several types of available smart phone geolocation techniques with varying levels of quality of service (QOS), which is also known as position accuracy (in meters) [62]. However, the tradeoff for better position accuracy is generally an increased response time (in seconds) to determine the smart phone's position. Within the LTE positioning protocol standard, the three defined techniques are enhanced

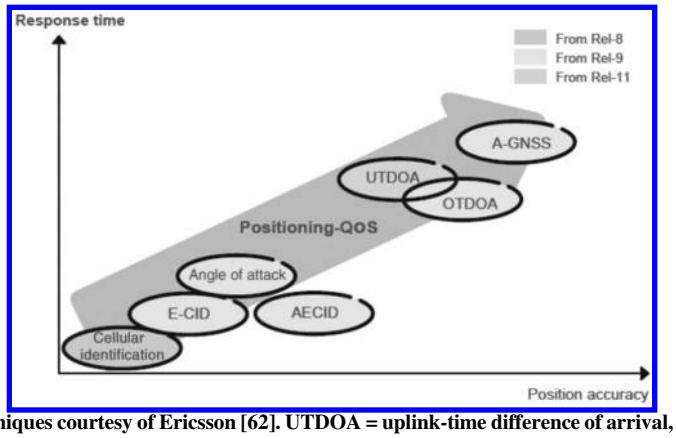

Fig. 4 Smart phone geolocation techniques courtesy of Ericsson [62]. UTDOA = uplink-time difference of arrival, AECID = adaptive enhanced cellular identification, Rel-8 = release 8, Rel-9 = release 9, Rel-11 = release 11.

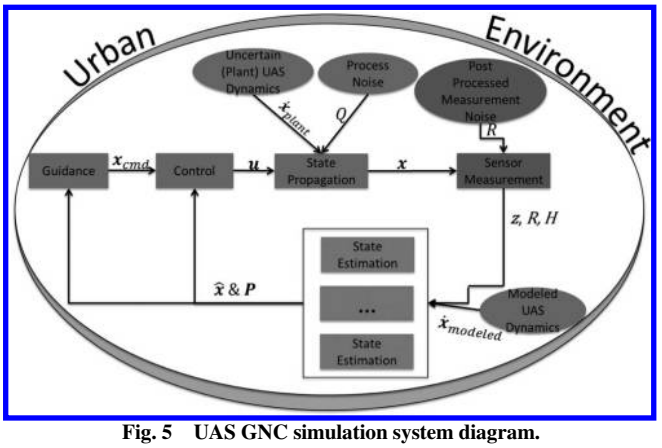

Fig. 5 UAS GNC simulation system diagram.

cellular identification (E-CID), observed time difference of arrival (OTDOA), and assisted–global navigation satellite system (A–GNSS) [63]. Since OTDOA is independent of GPS, more accurate than E-CID [64], and an active area of research [65], it is used in this research.

The OTDOA technique uses multilateration (hyperbolic lateration) to determine the position of the smart phone. The process is initiated when either the phone or the network requests an estimate of the position of the phone. Signals are then sent to the phone from at least three available towers, and the difference in arrival time for each pair of signals is calculated by the phone. It then sends this information to the network to generate a position update, or it can complete the calculation itself under certain conditions. The accuracy generally increases as a function of the number of available towers [60,66,67], up through 18 available towers. Since the urban environment generally has a large number of towers, it would provide the ideal situation for urban navigation. Simulation data show horizontal position errors ranging from 14.9 m with a standard deviation of 11.4 m for five available towers to 3.1 m with a standard deviation of 1.9 m for 30 available towers [60]. Although exact accuracy statistics are closely guarded by the companies developing this technology, Polaris Wireless currently advertises a 4 s Time to Fix with 40 m of accuracy.

C. Light Detection and Ranging

LIDAR is another navigation sensor that could possibly be used on small UAS in urban canyons, since it can operate in both bad weather and GPS degraded/denied conditions. It has been shown to increase urban canyon navigation accuracy by over an order of magnitude over the traditional GPS/IMU/odometry solution [68]. When tightly coupled with GPS/INS [32], it has also been shown to have submeter delta position accuracy in urban environments. However, these sensors have a high price tag of 2000 U.S. dollars at a minimum for a small low-cost UAS [69]. Their typical range of approximately 30 m limits the distance the UAS can fly from buildings to still effectively use this sensor [70].

III. Simulation Development

This section details the UAS guidance, navigation, and control simulation development within the framework seen in Fig. 5. It includes an overview of the simulation software, creation of the urban environment, the UAS controller and dynamics, the proposed sensor measurement generation algorithm, and a discussion of both the extended Kalman filter and the ensemble Kalman filter (ENKF).

A. Simulation Software Overview

Creating a realistic UAS guidance, navigation, and control (GNC) simulation requires a methodical system-level design with intuitive data structures. Using an easy-to-follow framework allows for both ease of use and a rapid customization capability. The UAS GNC simulation framework shown in Fig. 5 accomplishes that task, with each oval representing data inputs, whereas each block represents a GNC process described later in this section. Multiple state estimation blocks are shown to highlight this simulation's ability to incorporate different estimators.

B. Urban Environment Development

To navigate in an urban environment, simulations need to either use preloaded building and obstacle information, create their own urban environments based on incoming sensor data, or both. These environments can either be fictitious or based on real urban databases, such as the Primary Land Use Tax-Lot Output for the city of New York [71]. All landscapes developed using this tool assume, without loss of generality, that the landscape is aligned in a north–south manner with direction of travel from south to north. Figure 6 shows a representative generated urban environment, complete with sky bridges and antennas.

The UAS is assumed to have complete knowledge of the map to include all building, sky bridge, and antenna coordinates and heights, and the coordinates of the four corners of each block along with the heights of the tallest and shortest buildings on each block. This environment plays a critical role in determining the accuracy of the GPS and LTE sensor measurements used by the two state estimation filters.

C. UAS Dynamics Model and Controller

The nonlinear equations of motion for rigid-body fixed-wing UAS are in the form $\dot{\boldsymbol{x}} = f(\boldsymbol{x}, \boldsymbol{u})$, where $\boldsymbol{x}$ is the $n \times 1$ state vector and $\boldsymbol{u}$ is the $m \times 1$ control input vector:

$$\boldsymbol{x} = [x_N \quad x_E \quad h \quad V_T \quad \alpha \quad \beta \quad \phi \quad \theta \quad \psi \quad p \quad q \quad r]^T \tag{1}$$

The state vector shown in Eq. (1) consists of the inertial position coordinates: north position x_N; east position x_E; altitude h; airspeed V_t; angle of attack α; angle of sideslip β; the following Euler orientation angles of roll angle ϕ, pitch angle θ, and yaw angle ψ; and the body-fixed angular velocities of roll rate p, pitch rate q, and yaw rate r:

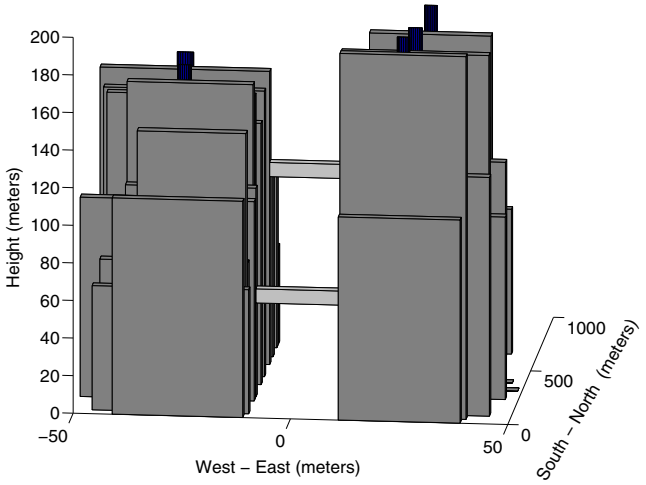

Fig. 6 Representative urban environment viewing from South to North.

$$\boldsymbol{u} = [\delta_a \quad \delta_e \quad \delta_r \quad F_T]^T \tag{2}$$

The control input vector shown in Eq. (2) consists of the aileron deflection δ_a, elevator deflection δ_e, rudder deflection δ_r, and thrust F_T. The full set of differential equations is available in chapter 3 of the work by Ducard, with aircraft model properties available in appendix F [72].

For control, a steady-state linear quadratic regulator (LQR) [73] is selected due to its straightforward implementation and constant gains when the UAS dynamics are linearized about a trim (steady flight) condition. These gains are shown in the appendices. The controller uses Eq. (3) as its control law, where $\boldsymbol{x}_{\text{cmd}_k}$ is the current commanded state vector, $\hat{\boldsymbol{x}}_{k-1}$ is the previous estimated state vector, and $\boldsymbol{u}_{\text{trim}}$ is the trim control input vector:

$$\boldsymbol{u}_k = \bar{K}(\boldsymbol{x}_{\text{cmd}_k} - \hat{\boldsymbol{x}}_{k-1}) + \boldsymbol{u}_{\text{trim}} \tag{3}$$

Since the longitudinal position cannot be directly commanded, the commanded state vector dimension is 11.

D. Sensor Measurement Generation

Figure 7 shows a system diagram of the possible sensors and existing urban canyon navigation solutions. The postprocessed sensor output noise characteristics are shown with solid lines, and the integrated system output noise characteristics are shown as dotted lines. Each sensor is currently available commercial off the shelf (COTS), and the integrated systems are available either as COTS or can be created using existing filtering techniques. The vision signal is considered to be the measurements directly from a vision system using odometry, localization, or both.

The available postprocessed measured states for each sensor are shown in Table 1. Inertial airspeed components are also available for GPS/IMU, but they are represented in the table as V_T to be consistent with the previously defined states. With this architecture, sensor specifications can be easily modified to account for changes in performance.

When a sensor measurement is available, it is generated using Eq. (4), where $\boldsymbol{v}_k \sim \mathcal{N}(0, R_k)$, with R_k as the measurement noise covariance matrix. The simplified model is used to allow focus on the state estimation process using several different sensors rather than the detailed modeling of any individual sensor:

$$\boldsymbol{z}_k = H_k \boldsymbol{x}_k + \boldsymbol{v}_k \tag{4}$$

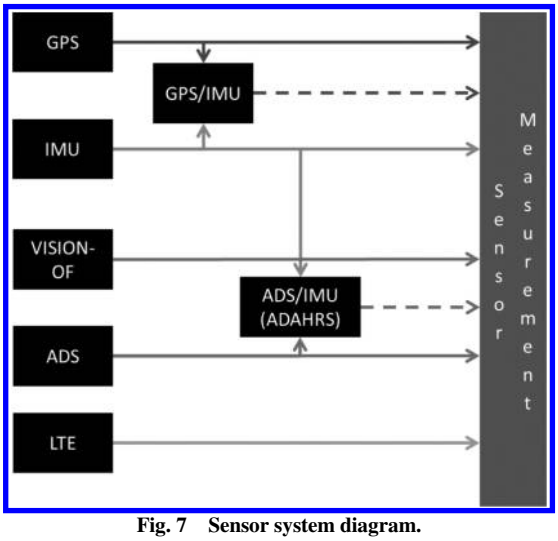

Fig. 7 Sensor system diagram.

Table 1 UAS sensor information

Sensor	Measured states
GPS	x_N, x_E, h, V_T
AHRS	$\phi, \theta, \psi, p, q, r$
Vision	V_T
ADS	h, V_T, α, β
LTE	x_N, x_E
GPS/IMU	$x_N, x_E, h, V_T, \phi, \theta, \psi, p, q, r$
ADS/IMU	$V_T, \alpha, \beta, \phi, \theta, \psi, p, q, r$

Table 2 Measurement noise covariance lookup table for GPS and LTE

	SL-1	SL-2	SL-3
ALT-1	σ_{11}^2	σ_{12}^2	σ_{13}^2
ALT-2	σ_{21}^2	σ_{22}^2	σ_{23}^2
ALT-3	σ_{31}^2	σ_{32}^2	σ_{33}^2

Some sensors such as an IMU or ADS have measurement noise covariance values that are determined through experimental testing. These values are not generally environment specific, so they can be set as constant values for both the measurement generation block and the state estimation filter block of Fig. 5. Sensors such as GPS, LTE, and vision require data manipulation to determine the most accurate measurement noise covariance values at a given time step. GPS and LTE have measurement noise covariances that are dependent on the environment. This is because GPS measurement accuracy is largely a function of satellite visibility among other factors [74], which is affected by the density of buildings and other structures. The same is true conceptually for LTE, since its accuracy is a function of the number of available towers, which is also dependent on the density of buildings and other signal blocking structures. In this paper, neither GPS nor LTE measurement accuracy was modeled as continuously time varying, since the paper's focus is not the specific temporal characteristics of each sensor's measurements but rather how the measurements are fused in different urban environments. Sensor availability and covariance are instead switched over a discrete value set as a function of the altitude and position in the urban canyon as described in the following.

An initial model to represent the variability in measurement noise values is shown in Table 2, which assigns a value based on the relative location of the UAS within the urban environment using published results from the literature.

The ALT and SL headings in Table 2 are the vertical and lateral descriptions, respectively, of the UAS with respect to the urban environment. ALT describes the UAS altitude (ALT) with respect to buildings, shown in Fig. 8; and SL describes the UAS street-level (SL) projection onto a two-dimensional map, shown in Fig. 9.

To determine the UAS ALT category, its altitude is compared to the tallest building along the current city block or intersection it is traversing. The UAS is in the ALT-1 category (Fig. 8a) when its altitude is higher than the tallest building on the current block or the buildings bordering the intersection. It is in the ALT-2 category (Fig. 8b) when its altitude is higher than the shortest building on the block/intersection but lower than the tallest building on that block/intersection. It is in the ALT-3 category (Fig. 8c) when it is lower than the shortest building on the block/intersection.

The UAS SL category is determined by comparing its lateral position to the surrounding buildings along the current block. It is in the SL-1 category when it is along a block with buildings on both sides of the street (Fig. 9a). It is in the SL-2 category when between canyons in an intersection between city blocks (Fig. 9b). The UAS is in the SL-3 category when there are only buildings on one side of the current block (Fig. 9c). Although the true measurement noise covariance model is most likely continuous and would need to be experimentally determined, this initial model is representative of the changing noise throughout the environment.

The optical flow measurement noise standard deviation σ_{pixels} is generally reported in units of pixels per frame, making a conversion to meters per second necessary. This is done by first determining the width W of the captured image presuming the camera's focal length f is known; the

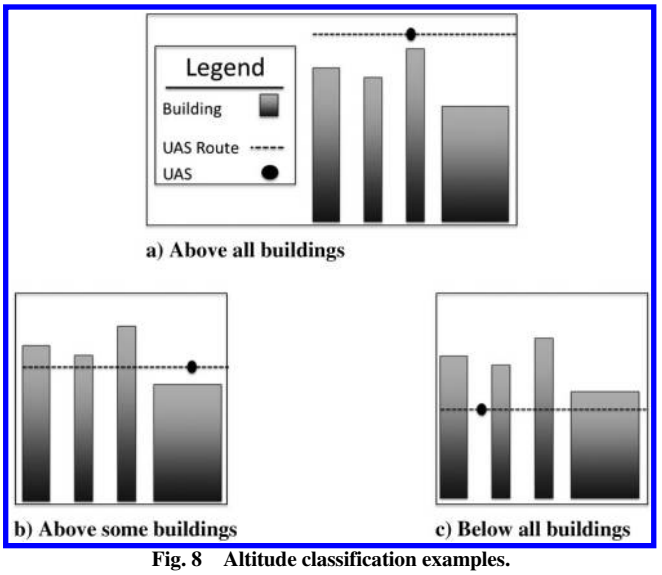

Fig. 8 Altitude classification examples.

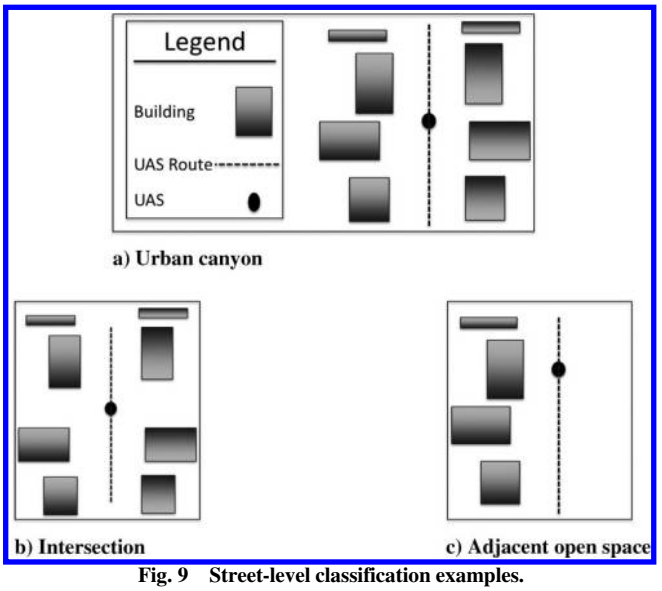

Fig. 9 Street-level classification examples.

image width is calculated with a pinhole camera assumption using Eq. (5), where L is the perpendicular distance from the camera to the real-world object, d is the horizontal dimension of the image, and f is the focal length of the lens:

$$W = \frac{L * d}{f} \tag{5}$$

The optical flow*based inertial airspeed noise covariance value assuming zero wind is then scaled from squared pixels per frame to squared meters per second using Eq. (6), where FR is the camera frame rate in frames per second and HR is the camera horizontal resolution in pixels. The σ_{pixels} used in this work is 4.54 pixels per frame, with a frame rate of 0.15 s and horizontal resolution of 752 pixels that are each 24 μm wide:

$$\sigma_{\text{OF}}^2 = \left(\frac{\sigma_{\text{OF}_{\text{pixels}}} FR * W}{HR}\right)^2 \tag{6}$$

E. State Estimation

State estimation filters enable feedback control for real-world systems. Bayesian filters accomplish this task through the use of a prediction-correction structure where the estimated state vector is propagated forward with a process model and then corrected using available measurements. Since the UAS dynamics are in the form of Eq. (7), where $\boldsymbol{x}(t)$ is the state of the system at a given time, $\boldsymbol{u}(t)$ is the control input at a given time, and the unknown process (plant) noise is $\boldsymbol{w}(t) \sim \mathcal{N}(0, Q(t))$, a nonlinear filtering techniques such as the EKF and ENKF can be used:

$$\dot{\boldsymbol{x}}(t) = f(\boldsymbol{x}(t), \boldsymbol{u}(t))) + \boldsymbol{w}(t) \tag{7}$$

1. *Extended Kalman Filter*

The EKF, a nonlinear extension of the Kalman Filter [75,76], linearizes the system dynamics [Eq. (7)] and the measurement model [Eq. (4)] at each instance in time about the most recent estimated state and control input vectors [77]. A posterior Gaussian distribution is maintained to allow the estimated state vector and covariance matrix to be calculated using a process almost identical to that of the Kalman Filter.

The initial estimated state vector $\hat{\boldsymbol{x}}_0$ is drawn from $\mathcal{N}(\boldsymbol{x}_0, P_0)$, where $\boldsymbol{x}_0$ is the known initial true state vector and P_0 is the known initial covariance matrix. The predicted estimated state vector $\hat{\boldsymbol{x}}_k^-$ and predicted covariance matrix P_k^- are then calculated using Eqs. (8) and (9). Since aircraft dynamics are typically written as differential equations, a technique such as the Runge–Kutta fourth-order method can be used for propagation:

$$\hat{\boldsymbol{x}}_k^- = f(\boldsymbol{x}_{k-1}, \boldsymbol{u}_{k-1}) \tag{8}$$

$$P_k^- = A_{k-1} P_{k-1} A_{k-1}^T + Q_k \tag{9}$$

Once the available measurement vector z_k, calculated using Eq. (4), is received at the current time step, the filter calculates the corrected estimated state vector $\hat{\boldsymbol{x}}_k$ and the corrected covariance matrix P_k shown in Eqs. (10) and (11), respectively:

$$\hat{\boldsymbol{x}}_k = \hat{\boldsymbol{x}}_k^- + K_k \nu_k \tag{10}$$

Table 3 Simulation test matrix

Test identification	Environment	Altitude h	Available sensors
1	Open space	125 m	AHRS, ADS, GPS
2	Open space	125 m	AHRS, IMU, ADS, GPS, LTE
3	High canyon	75 m	AHRS, IMU, ADS, GPS, LTE, vision-OF x 2
4	Low canyon	50 m	AHRS, IMU, ADS, LTE, vision-OF x 2
5	Varies	Sinusoidal-up (75 m)	AHRS, IMU, ADS, GPS, LTE, vision-OF x 2
6	Varies	Sinusoidal-down (75 m)	AHRS, IMU, ADS, GPS, LTE, vision-OF x 2

$$P_k = (I - K_k H_k) P_k^- \tag{11}$$

2. Ensemble Kalman Filter

In contrast with the EKF, which uses a recursive calculation of the estimated state vector mean and covariance to represent the posterior belief distribution of each unobservable state, particle filters use an ensemble of N_p samples or particles to represent the distribution [78], where each particle is drawn as shown in Eq. (12). In this type of filter, only the ensemble is calculated recursively:

$$\boldsymbol{x}_k^i \sim p(\boldsymbol{x}_k | z_{1:\,k}, \boldsymbol{u}_{1:\,k}) \tag{12}$$

The ENKF, introduced in [79], is a variant of the particle filter in which all distributions are assumed to be Gaussian. The ensemble is formed as $\boldsymbol{X}_k = \{\boldsymbol{x}_k^1, \boldsymbol{x}_k^2, \ldots, \boldsymbol{x}_k^N\}$ with increasing accuracy as $N \to \infty$. Similar to the EKF, the ENKF includes both prediction and correction steps, which are called the forecast step and the analysis step, respectively. The ENKF filtering process [80] is initialized by drawing N particles from $\mathcal{N}(\boldsymbol{x}_0, P_0)$ to form the initial ensemble. Each of these particles is propagated during the forecast step using Eq. (13) to form X_k^{i-}, where $w_k^i \sim \mathcal{N}(0, Q_k)$:

$$\boldsymbol{x}_k^{i-} = f(\boldsymbol{x}_{k-1}^{i-}, \boldsymbol{u}_{k-1}) + \boldsymbol{w}_k^i \tag{13}$$

The forecast state vector is created by calculating the ensemble mean using Eq. (14). The state error vector ensemble is calculated using Eq. (15), and the forecast estimated state vector covariance is calculated using Eq. (16):

$$\hat{\boldsymbol{x}}_k^- = \frac{1}{N_p} \sum_{i=1}^{N_p} \boldsymbol{x}_k^{i-} \tag{14}$$

$$E_{xk}^- = [\boldsymbol{x}_k^{1-} - \hat{\boldsymbol{x}}_k^- \ldots \boldsymbol{x}_k^{N-} - \hat{\boldsymbol{x}}_k^-] \tag{15}$$

$$P_k^- = \frac{E_{xk}^- E_{xk}^{-T}}{N_p - 1} \tag{16}$$

In the analysis step, N_p particles in the ensemble are corrected given the available measurement vector using Eq. (17) with the estimated state vector mean calculated using Eq. (18). Gillijns et al. [80] provided more details on the intermediate calculations used in generating the corrected estimate and covariance for the ENKF:

$$\boldsymbol{x}_k^i = \boldsymbol{x}_k^{i-} + K_k N_k^i \tag{17}$$

$$\hat{\boldsymbol{x}}_k = \frac{1}{N_p} \sum_{i=1}^{N_p} \boldsymbol{x}_k^i \tag{18}$$

Delay compensation is necessary for GPS and LTE measurements, since they both become available at a later time than they are acquired. GPS measurements are delayed 0.1 s according to [36] and LTE measurements are delayed between 4 and 10 s according to the Polaris Wireless website[‡] and [64]. A common technique to properly account for measurement delay is state augmentation or stochastic cloning [81,82]. A brief summary of state augmentation is discussed here, with more details in [81]. For a measurement with a known delay of m time steps that becomes available at time step k, state augmentation keeps a copy of the estimated state vector at time step $(k - m)$ and appends it to the bottom of the estimate state vector until time k while expanding the estimated state covariance matrix accordingly. As the estimated state vector is propagated forward, the augmented states are not propagated but are adjusted as the augmented covariance matrix is corrected using intermediate measurements. At time step k, the simulated time-delayed measurement (i.e., measurement acquired using true state vector at time step $k - m$) and augmented estimated state vector are used to calculate the augmented innovation vector. Once the filter has completed the correction step at time step k, the augmented states and their associated covariance matrix entries are marginalized out of the system and the process is repeated for the next measurement from the delayed sensor.

[‡]Available online at http://www.polariswireless.com/.

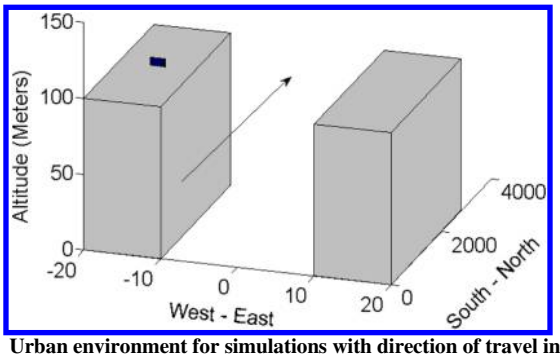

Fig. 10 Urban environment for simulations with direction of travel indicated.

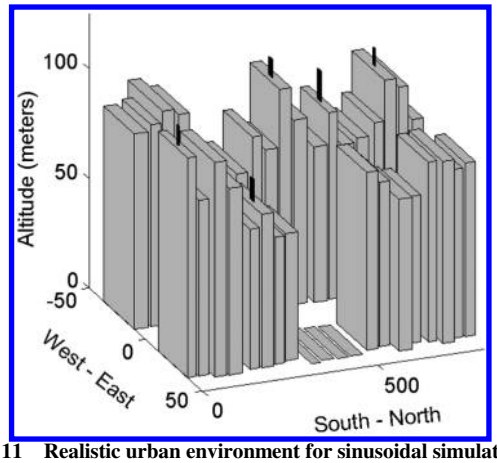

Fig. 11 Realistic urban environment for sinusoidal simulations.

IV. Simulation Execution

A. Test Matrix

Four tests, as shown as tests 1–4 in Table 3, were conducted to explore the effects of GPS, vision-optic flow (OF), and LTE in the simple and consistent urban environment depicted in Fig. 10. Two additional sinusoidal trajectory tests (test 5 and 6) were conducted in a realistic urban environment, as shown in Fig. 11. It was assumed that the UAS was equipped with a vision sensor along both wings, as denoted by "x 2" in Table 3 for vision-OF.

Test 1 served as a baseline using currently available sensors with published accuracy in an open space where vision systems would not produce useful information. Test 2 was conducted in the same environment but added the LTE sensor to determine what if any effect it had on navigation accuracy.

Tests 3 and 4 explored navigation accuracy degradation when using optical flow only. All tests were conducted both with and without sensor delay to show the effect of sensor delay on the system.

B. Simulation Parameters

To conduct the tests in Table 3, the available measurements, sampling rates, sampling delays, and measurement noise covariance values (with the exception of GPS and LTE) for each sensor are defined in Table 4. GPS and LTE noise covariance values are shown in Tables 5 and 6, respectively. Each was taken from published results or sensor/integrated system specification sheets. A complete listing of values is shown in Table A1 of Appendix A to this paper.

Since each sensor measures a different set of states, none fully observes the state of the system at any given time. Because of this, estimates of some of the states, such as the three-dimensional inertial position provided by GPS and LTE, are generally made without current measurement data. This lack of available measurements causes an increase in estimate uncertainty in an environment that generally has little margin for navigation errors. However, AHRS measurements are available at every time step, allowing accurate estimates of these states with little uncertainty.

The vision-OF inertial airspeed noise covariance is converted to meters per second using specifications from the PX4FLOW Smart Camera, which is a typical optical flow camera available on hobby Web sites, The PX4FLOW has a resolution of 752×480 with a 16 mm focal length and 24×24 μm pixel size. The optical flow algorithm accuracy and computational speed data shown in Table 4 are taken from the Bartels and De Haan algorithm [83] published in the Middlebury Optical Flow Evaluation results for synthetic urban images [84].

GPS ALT-1 measurement noise covariance values were taken from work by Beard and McLain [43] and u-blox [42], whereas ALT-3/SL- values were taken from work by MacGougan et al. [46]. The remaining position values were interpolated, and the airspeed noise covariance value was taken from work by Langelaan et al. [38]. LTE OTDOA noise covariance values were generated from [85], as this was the only identified source of LTE positioning accuracy as a function of the number of available towers. The simulation capped accuracy at 20 available towers, consistent with a review of the Cell Reception website[§] for Detroit, Michigan, which indicated 22 cellular towers in and around the downtown core. All towers were presumed to be on the LTE network.

Table 7 shows the general simulation parameters, including time step, simulation length, number of Monte Carlo runs, and the number of particles when using the ENKF.

[§]Available online at http://www.cellreception.com/coverage/mi/detroit/page1.html.

Table 4 Sensor simulation parameters

Sensor	Sampling rate, Hz	Sampling delay, s	Measured states (noise covariance values)
GPS	1	0.1	x_N, x_E, h, V_T (see Table 5)
Vision-OF inertial airspeed only	6.67	0.15	V_T [4.54 frames/s]^2
AHRS	100	0	ϕ, θ, ψ [2.71 deg, 1.65 deg, 8.27 deg]^2, p, q, r [0.6 deg/s, 0.6 deg/s, 0.6 deg/s]^2
ADS	50	0	h, V_T, α, β [1.5 m, 1 m/s, 1 deg, 1 deg]^2
LTE	1/4	4	x_N, x_E (see Table 6)

Table 5 Location-based GPS receiver noise covariance data

	$\sigma^2_{x_{N,E/h}}(\mathrm{m}_2)$		
	SL-1	SL-2	SL-3
ALT-1	$3.67^2/7.2^2$	$3.67^2/7.2^2$	$3.67^2/7.2^2$
ALT-2	$6.96^2/19.59^2$	$6.45^2/17.99^2$	$5.68^2/15.60^2$
ALT-3	$10.25^2/31.98^2$	$9.23^2/28.78^2$	$7.69^2/23.99^2$

Table 6 Location-based LTE noise covariance data

	$\sigma^2_{x_{N,E}}(\mathrm{m}_2)$ (number of available towers)		
	SL-1	SL-2	SL-3
ALT-1	4.38 (10–15)	4.38 (10–15)	4.38 (10–15)
ALT-2	4.38 (10–15)	3.48 (15–20)	4.38 (10–15)
ALT-3	6.26 (7–10)	4.38 (10–15)	6.26 (7–10)

Table 7 General simulation parameters

Parameter	Value
Time step dt	0.01 s
Simulation length	20 s (600 m)
Number of Monte Carlo runs	500
Number of particles N_p	1000

Table 8 Initial true state and initial covariance values

State	Initial true value	Initial covariance	State	Initial true value	Initial covariance
x_N	5 m	$(1\ \mathrm{m})^2$	ϕ	0.0003 rad	$(1\pi/180\ \mathrm{rad})^2$
x_E	0 m	$(1\ \mathrm{m})^2$	θ	0.0893 rad	$(1\pi/180\ \mathrm{rad})^2$
h	Varies per test	$(1\ \mathrm{m})^2$	ψ	0.0005 rad	$(1\pi/180\ \mathrm{rad})^2$
V_T	30 m/s	$(0.5\ \mathrm{m/s})^2$	p	0 rad/s	$(1\pi/180\ \mathrm{rad})^2$
α	0.0893 rad	$(1\pi/180\ \mathrm{rad})^2$	q	0 rad/s	$(1\pi/180\ \mathrm{rad})^2$
β	0.0003 rad	$(1\pi/180\,\mathrm{rad})^2$	r	0 rad/s	$(1\pi/180\ \mathrm{rad})^2$

C. State Estimation Filter Initialization

The initial true UAS state vector and diagonal covariance matrix values are shown in Table 8 for a steady-level trim flight condition. For both filters, the initial estimated state vector for each Monte Carlo simulation was drawn from $\mathcal{N}(\boldsymbol{x}_0, P_0)$. The constant process noise covariance matrix Q was set to $10^{-4} * I_{12}$.

V. Results

A. Open Space

Table 9 shows the longitudinal and lateral RMS position error values at the final time step for the two open-space test environments. For both filters, the position error is similar with and without the LTE measurement. However, in the no-delay case, the LTE measurement slightly aids in decreasing the longitudinal error, whereas it causes a slight error increase in the delayed case for both filters. The difference in the magnitude of the lateral and longitudinal errors in the open-space environments is due to the controller constantly attempting to correct the lateral position back to the center of the canyon. This causes small overshoots of the trim position throughout the duration of the simulation. The ENKF did not show any

Table 9 RMS position error at $t = 20$ s for open-space test environments

	EKF (no delay)		EKF (delay)		ENKF (delay)	
Environment	x_N, m	x_E, m	x_N, m	x_E, m	x_N, m	x_E, m
Open space (no LTE)	0.67	1.23	0.66	1.24	0.67	1.32
Open space	0.64	1.25	0.71	1.19	0.68	1.35

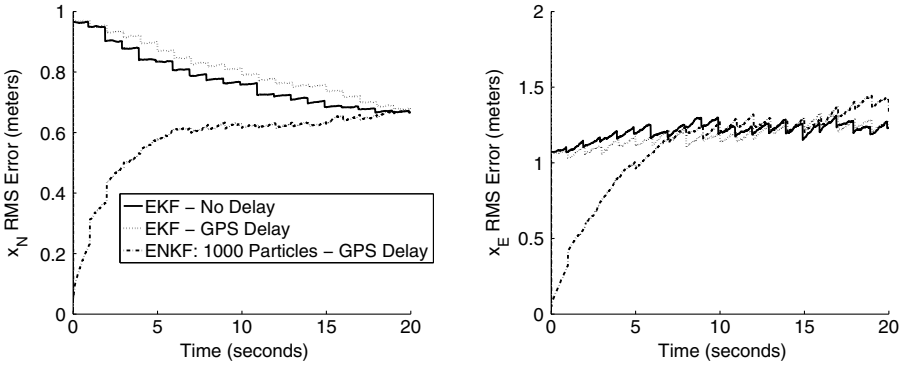

a) Longitudinal position **b) Lateral position**

Fig. 12 RMS error trajectory for open-space environment with GPS.

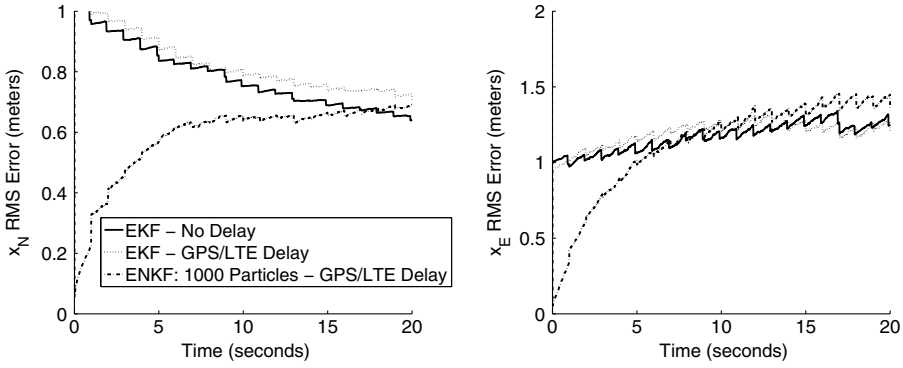

a) Longitudinal position **b) Lateral position**

Fig. 13 RMS error trajectory for open-space environment with GPS and LTE.

improvement in longitudinal or lateral position errors, as it was simply calculating the estimated state vector and covariance empirically instead of closed form in order to eliminate the need to generate the state transition Jacobian. Note that both the EKF and ENKF initial state estimates were specified over the same initial distribution centered on the true initial state vector. However, since the EKF only draws one sample from the initial distribution for each Monte Carlo run while the ENKF draws 1000 samples for each run, the ENKF initial RMS error will average to a value much closer to zero.

Figures 12 and 13 show the horizontal RMS position error trajectories of the two open-space environments. The RMS position error trajectories are similar for both states when the EKF is used. The sawtooth pattern in the lateral states resulted from measurements being received to decrease error but an overall increasing error as the controller constantly overshot the commanded position value. The addition of LTE, with its 4 s delay, did not give any better performance, since these measurements were not weighted as highly as the less-delayed GPS measurements in the correction step. The ENKF gives a much lower initial RMS error for both states because it is able to average the entire initial ensemble. However, the error increases to EKF levels during the simulation as the forecasted mean is propagated with process noise. In both environments, the delayed EKF and ENKF longitudinal position errors approach the same value, showing that, in a steady-level trajectory with a nearly constant state transition matrix, the EKF is tough to outperform.

Although the LTE measurements had little effect on increasing the accuracy of the position estimate, they did slightly increase confidence in the estimate, as shown in Fig. 14. Here, the EKF and ENKF position error 3σ bounds are shown for the longitudinal position state (Fig. 14a) and the lateral position state (Fig. 14b). The dotted lines represent the open-space environment with GPS only using the EKF (outer) and ENKF (inner).

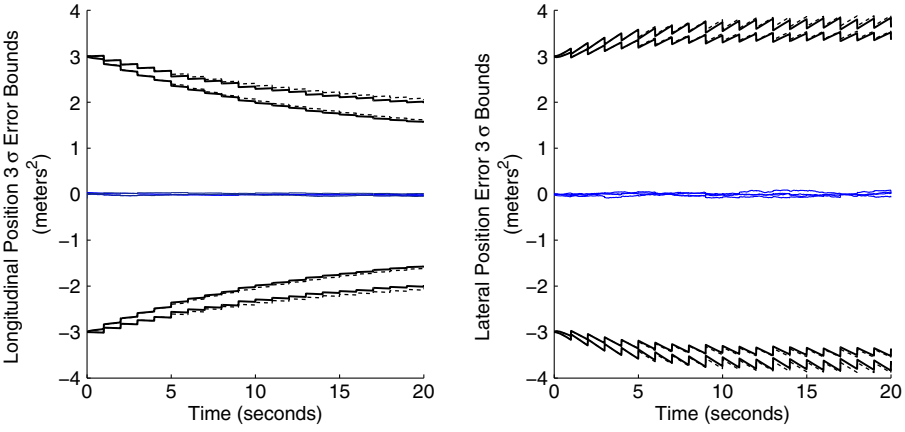

a) Longitudinal position **b) Lateral position**

Fig. 14 Effect of adding delayed LTE sensor on horizontal position error 3σ bounds.

Table 10 RMS position error at $t = 20$ s for canyon test environments

	EKF (no delay)		EKF (delay)		ENKF (delay)	
Environment	x_N, m	x_E, m	x_N, m	x_E, m	x_N, m	x_E, m
High canyon (vision-OF)	0.89	1.73	0.92	1.79	0.74	1.93
Low canyon (vision-OF/no GPS)	0.98	1.88	1.01	2.06	0.78	2.21

The solid lines represent the open-space environment with the delayed LTE measurements added to the GPS using the EKF (outer) and ENKF (inner). The increase in estimate confidence is shown by the slight divergence of the solid and dotted lines, with small but noticeable shrinking of the bounds when the first delayed LTE measurement arrives at the 5 s point as more measurement information is received by the filter. Also, as expected, the ENKF does give tighter bounds, since the covariance is empirically calculated and more closely approximating the true error of the system.

B. Canyons

Table 10 shows the longitudinal and lateral RMS position error value at the final time step for the four canyon test environments. Vision-OF provides airspeed updates such that longitudinal and lateral RMS errors are approximately 1 m and 2 m, respectively, in realistic delayed measurement cases. Although the ENKF performed slightly better in the longitudinal direction with RMS errors just under 0.8 m, the lateral position error became slightly worse as in the open-space tests as it attempted to keep the UAS on the canyon centerline with less accurate, low-sampling rate, delayed measurements.

For vision-OF, the results are shown in Figs. 15 and 16 for the high and low canyon environments. These results show the same trends as the open-space results, since the only position sensors are GPS and LTE in the high canyon and only LTE in the low canyon. However, the RMS errors are higher, especially when using the EKF, because the GPS measurements are less accurate, when available, and the LTE measurements are only available every 4 s and are delayed by 4 s. This effect is seen more in the lateral position errors as the controller attempts to center the UAS using this delayed measurement. The ENKF does provide a more accurate initial estimate of the longitudinal position with these low sampling rate sensors, but it degrades over time and is still increasing at 20 s. Overall, GPS and/or LTE can only provide a roughly 1 m RMS error (RMSE) in longitudinal position estimation within an urban canyon as the RMS error in the lateral position estimate continuously degrades.

C. Sinusoidal Flight Path

For tests 5 (initial climb) and 6 (initial descent), the UAS flew a sinusoidal flight path through a realistic urban canyon. Figure 17 shows the horizontal position RMSE trajectories when the UAS has an initial altitude of 75 m. Results from a constant 75-m-altitude flight-path simulation are included for reference. For longitudinal and lateral position error trajectories in Figs. 17a and 17b, the initial descent flight path outperforms

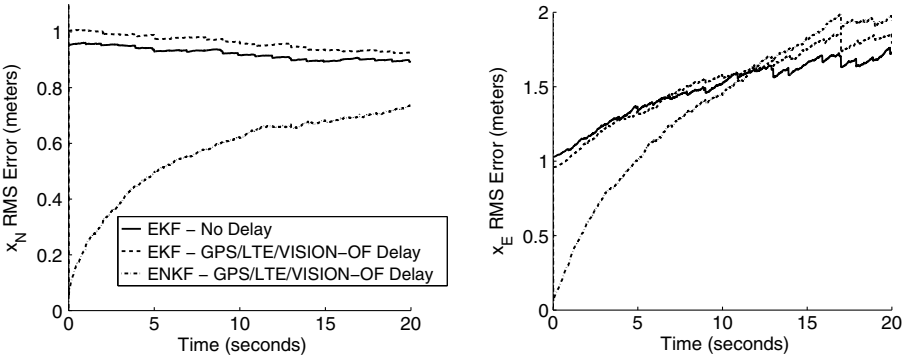

a) Longitudinal position **b) Lateral position**

Fig. 15 RMS error trajectories for high canyon environment with GPS, LTE, and vision-OF.

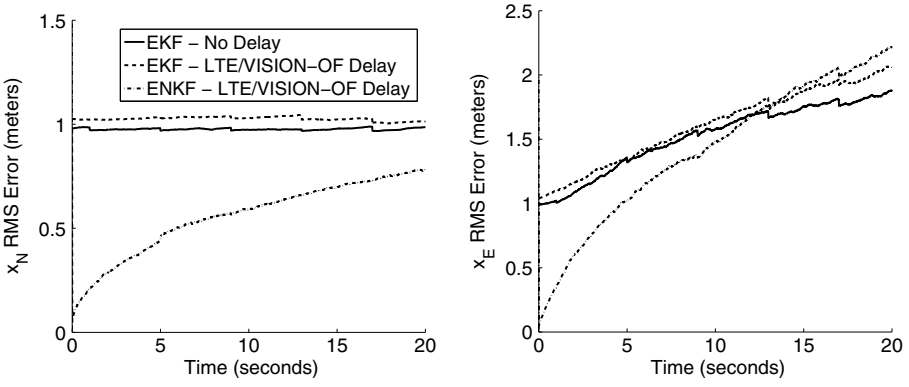

a) Longitudinal position **b) Lateral position**

Fig. 16 RMS error trajectories for low canyon environment with LTE and vision-OF.

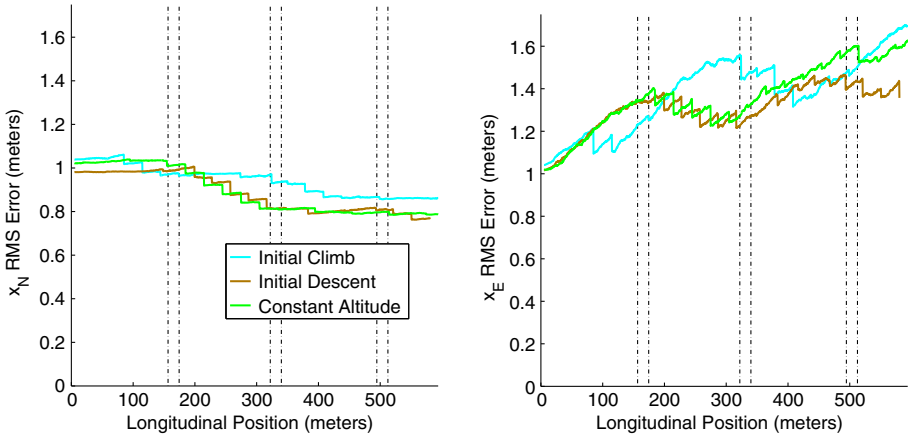

a) Longitudinal **b) Lateral**

Fig. 17 Horizontal position RMSE trajectories for sinusoidal trajectories through the urban environment where $h_0 = 75$ m.

both the climbing flight path and the constant-altitude flight path. This is due to the UAS being above all buildings for all of the second canyon where the climbing flight is primarily below building tops in the this canyon. In the lateral case, the climbing flight path has a sharp drop in error during the first half of the third canyon as it climbs above the tops of all buildings, but this is brief as it descends back into the canyon and its lateral error linearly increases. Even though a UAS may not fly these exact sinusoidal flight paths through the canyon, the noticeable trend is that rapid changes in altitude induce rapid changes in RMS error as GPS measurements are lost and gained.

VI. Conclusions

In this paper, candidate urban navigation sensors and filtering techniques were characterized and evaluated. A modular UAS urban navigation simulation framework was proposed, enabling systematic tests of postprocessed sensor measurement fusion using both an extended Kalman filter and an ensemble Kalman filter. GPS and LTE environment-dependent measurement noise categories were presented to account for the role of the urban environment as a factor in their noise values. Since vision-OF only provides an airspeed measurement in a canyon, it must also be augmented with another inertial position measurement sensor to provide adequate navigation accuracy. In this case, addition of LTE was not sufficient, as it had little effect on increasing or decreasing the RMS horizontal position error. However, it did cause the covariance bounds to shrink slightly. Should LTE technology mature to the point where its delay is substantially decreased, it can have a more beneficial effect on the navigation system in the absence of reliable GPS.

Future work will include exploring LTE further to determine the sampling frequency increase and corresponding delay decrease needed to show increased performance. Also, transitions between categories of urban environments will be studied to determine how estimation error and confidence bounds change during these sensor crossover periods, especially with the temporary loss of vision system measurements in intersections. Wind models will be added to the UAS plant dynamics to better match the realistic conditions in an urban environment. Wind can gust and can change direction quickly when deflected by buildings, billboards, overpasses, and other structures with noticeable impact on UAS motion. Lastly, flight testing should be conducted to validate predictions; such testing is feasible once policy supports it, since most of the referenced sensors have already been integrated onto small, lightweight commercial-off-the-shelf autopilots. The integration of a low-weight dual camera system and LTE transceiver would be necessary, but they could be hosted on existing small UAS platforms.

Appendix A: Published Sensor and Integrated System Noise Values

Table A1 summarizes the literature survey of sensor and integrated sensor system noise. The information in Table A1 was gathered from publications including sensor specification sheets, sensor user manuals, conference proceedings, journal articles, dissertations, and books. All values shown with an asterisk (*) have been processed by the authors, either by averaging experimental data or interpolating plots.

Table A1 UAS sensor accuracy survey

Measured state	Sensor type	1σ noise value	Source
x_N, x_E, h, m	GPS	$3, 0.5, 3(h = 2), 3.67^*$	[38], [39], [57], [43]
	GPS/IMU	4.05/1.26/3.07	[44]
	Vision/IMU	0.36/0.31/0.33	[27]
h, m	ADS	10	[54]
	Altimeter	0.4, 1.5, 3	[39], [56], [57],
V_T, m/s	GPS	0.1, 0.01	[38], [86]
	ADS	0.2, 0.4, 1.5, 1	[87], [39], [57], [88]
α, β, deg	ADS	1/1, 1/1	[87], [54]
	Pitot tube/IMU	1.8/0.95	[89]
ϕ, θ, ψ, deg	AHRS	$2/2/2, 1.65/2.71/-^*$	[41], [34], [37]
	GPS/IMU	$3, 0.87^*/1.17^*/4.20^*, 2.08/2.21/8.27$	[36], [57], [86]
		$0.78/0.80/-$	[45]
	Vision/IMU	$1.52/1.78/-$	[29]
p, q, r, deg /s	IMU	$0.57, 0.29, 0.66^*$	[38], [39], [40]

Appendix B: Ensemble Kalman Filter Gain Approximation

In [80], K_k is calculated using Eqs. (B1) and (B2) to approximate $P_k^- H_k^T$ and S_k, respectively, where z_k^i is the ith column in $\boldsymbol{Z}_k$ and $\bar{z}_k$ is the measurement mean:

$$P_{xzk} = \frac{E_{xk}^-[z_k^1 - \bar{z}_k \ldots z_k^N - \bar{z}_k]^T}{N_p - 1} \tag{B1}$$

$$P_{zzk} = \frac{[z_k^1 - \bar{z}_k \ldots z_k^N - \bar{z}_k][z_k^1 - \bar{z}_k \ldots z_k^N - \bar{z}_k]^T}{N_p - 1} \tag{B2}$$

To test this Kalman gain matrix approximation, 100 Monte Carlo runs were conducted to calculate the Frobenius norm of the difference between the closed-form Kalman gain matrix and its approximation for the 12-state UAS equations of motion. Figure B1 shows the trajectory of the norm for $N_p = \{500, 1000, 5000, 10,000\}$ particles. The spikes in each trajectory represent the time step in which a delayed GPS

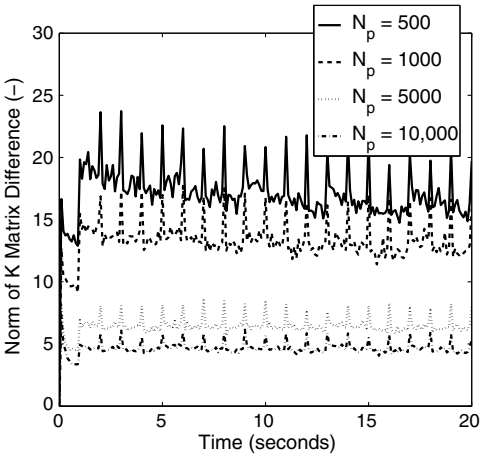

Fig. B1 Kalman gain matrix approximation error trajectory averaged over 100 Monte Carlo runs.

measurement was received. Although the norm of the difference decreases with the increase in number of particles, it reaches only a minimum of five when using a 10,000-particle ensemble. This level of error suggests this approximation would be more useful in smaller-dimension systems that have more precise measurements.

Appendix C: Linear Quadratic Regulator Controller Gain

Table C1 of this appendix contains the LQR gain matrices for the steady-level flight and wings-level descending flight trim conditions where $\bar{\rho} = 10$ for both matrices.

Table C1 UAS LQR controller gains for steady-level flight: $V_T = 30$ m/s, h = 50 m, and $\gamma = 0$ deg

	h	V_t	α	θ	q	β	x_E	ϕ	ψ	p	r
δ_a	−0.0003	0	0.0007	−0.0052	0	5.9738	0.2191	0.5757	6.6334	0.2436	0.1324
δ_e	0.3117	−0.0360	−2.1909	5.1431	0.4067	0.0025	0.0003	−0.0016	0.0056	0	0
δ_r	−0.0001	0.0001	−0.0005	−0.0030	0	5.6482	0.2280	0.1291	6.2553	0.0271	0.2713
F_T	13.7652	79.1967	−106.4399	54.3512	−2.4391	−0.7129	−0.252	−0.0350	−0.5947	−0.0016	0.0067

Acknowledgments

The authors would like to thank the U.S. Air Force Academy Department of Mathematical Sciences for selecting Justin Rufa to pursue a Ph.D. and the U.S. Air Force for allowing him to attend the University of Michigan to accomplish this mission.

References

[1] van Blyenburgh, P., "Unmanned Aircraft Systems: The Current Situation," *UAS ATM Integration Workshop*, UVS International, Paris, 2008.

[2] La Franchi, P., "Law Enforcement UAV Requirements Under Study by Thales UK," *Flight International*, July 2007, https://www.flightglobal.com/news/articles/law-enforcement-uav-requirements-under-study-by-thales-uk-215328/.

[3] Ma, C., Jee, G., MacGougan, G., Lachapelle, G., Bloebaum, S., Cox, G., Garin, L., and Shewfelt, J., "GPS Signal Degradation Modeling," *Proceedings of the 14th International Technical Meeting of the Satellite Division*, ION, Salt Lake City, UT, 2001, pp. 882–893.

[4] Prost, J., Godefroy, B., and Terrenoir, S., "City Walking: Improving GPS Accuracy for Urban Pedestrians," *GPS World*, Vol. 19, No. 8, 2008, pp. 32–37.

[5] Lu, M., Chen, W., and Chan, W., "Discussion of 'Building Project Model Support for Automated Labor Monitoring' R. Sacks, R. Navon, and E. Goldschmidt," *Computing in Civil Engineering*, Vol. 18, No. 4, 2004, pp. 381–383. doi:10.1061/(ASCE)0887-3801(2004)18:4(381)
[6] Grabowski, J., "Personal Privacy Jammers: Locating Jersey PPDs Jamming GBAS Safety-of-Life Signals," *GPS World*, Vol. 23, No. 4, 2012, p. 28.
[7] Hanlon, M., "DARPA's Surface Navigation Concept—Without GPS," *Gizmag*, April 2007, http://www.gizmag.com/go/7140/.
[8] Haigh, N., "BAE Systems Locates Opportunity to Replace GPS," 2012, http://www.baesystems.com/en-uk/article/bae-systems-locates-opportunity-to-replace-gps [accessed 27 December 2015].
[9] Mar, J., and Leu, J., "Simulations of the Positioning Accuracy of Integrated Vehicular Navigation Systems," *IEE Proceedings: Radar, Sonar and Navigation*, Vol. 143, No. 2, 1996, pp. 121–128. doi:10.1049/ip-rsn:19960222
[10] Mezentsev, O., Lu, Y., Lachapelle, G., and Klukas, R., "Vehicular Navigation in Urban Canyons Using a High Sensitivity GPS Receiver Augmented with a Low Cost Rate Gyro," *Proceedings of the GPS Conference*, Vol. 15, ION, Portland, OR, 2002, pp. 263–369.
[11] Vicek, C., McLain, P., and Murphy, M., "GPS/Dead Reckoning for Vehicle Tracking in the 'Urban Canyon' Environment," *Proceedings of the Vehicle Navigation and Information Systems Conference*, IEEE/IEE, Ottawa, ON, Canada, 1993. doi:10.1109/VNIS.1993.585671
[12] Georgy, J., Iqbal, U., and Noureldin, A., "Quantitative Comparison Between Kalman Filter and Particle Filter for Low Cost INS/GPS Integration," *Proceedings of the 6th International Symposium on Mechatronics and its Applications*, IEEE Publ., Piscataway, NJ, 2009, pp. 1–7.
[13] Hide, C., Moore, T., Hill, C., and Park, D., "Low Cost, High Accuracy Positioning in Urban Environments," *Journal of Navigation*, Vol. 59, No. 3, 2006, pp. 365–379. doi:10.1017/S0373463306003936
[14] Davidson, P., Hautamäki, J., Collin, J., and Takala, J., "Improved Vehicle Positioning in Urban Environment Through Integration of GPS and Low-Cost Inertial Sensors," *Proceedings of the European Navigation Conference*, EUGIN, Naples, Italy, 2009, http://www.eugin.info/?s=32,eugin+conferences.
[15] Cui, Y., and Ge, S., "Autonomous Vehicle Positioning with GPS in Urban Canyon Environments," *IEEE Transactions on Robotics and Automation*, Vol. 19, No. 1, 2003, pp. 15–25. doi:10.1109/TRA.2002.807557
[16] Drevelle, V., and Bonnifait, P., "iGPS: Global Positioning in Urban Canyons with Road Surface Maps," *IEEE Intelligent Transportation Systems Magazine*, Vol. 4, No. 3, 2012, pp. 6–18. doi:10.1109/MITS.2012.2203222
[17] Syed, S., "GPS Based Map Matching in the Pseudorange Measurement Domain," *Proceedings of the 17th International Technical Meeting of the Satellite Division of The Institute of Navigation*, ION, Long Beach, CA, 2004, pp. 241–252.
[18] Boucher, C., and Noyer, J., "A hybrid Particle Approach for GNSS Applications with Partial GPS Outages," *IEEE Transactions on Instrumentation and Measurement*, Vol. 59, No. 3, 2010, pp. 498–505. doi:10.1109/TIM.2009.2021238
[19] Georgy, J., Noureldin, A., and Goodall, C., "Vehicle Navigator Using a Mixture Particle Filter for Inertial Sensors/Odometer/Map Data/GPS Integration," *IEEE Transactions on Consumer Electronics*, Vol. 58, No. 2, 2012, pp. 544–552. doi:10.1109/TCE.2012.6227459
[20] Wei, W., Zongyu, L., and Rongrong, X., "INS/GPS/Pseudolite Integrated Navigation for Land Vehicle in Urban Canyon Environments," *Proceedings of the Conference on Cybernetics and Intelligent Systems*, Vol. 2, IEEE Publ., Piscataway, NJ, 2004, pp. 1183–1186.
[21] Kloeden, H., Schwarz, D., Biebl, E., and Rasshofer, R., "Vehicle Localization Using Cooperative RF-Based Landmarks," *Proceedings of the Intelligent Vehicles Symposium*, IEEE Publ., Piscataway, NJ, 2011, pp. 387–392.
[22] Lu, M., Chen, W., Shen, X., Lam, H., and Liu, J., "Positioning and Tracking Construction Vehicles in Highly Dense Urban Areas and Building Construction Sites," *Automation in Construction*, Vol. 16, No. 5, 2007, pp. 647–656. doi:10.1016/j.autcon.2006.11.001
[23] Muratet, L., Doncieux, S., Briere, Y., and Meyer, J., "A Contribution to Vision-Based Autonomous Helicopter Flight in Urban Environments," *Robotics and Autonomous Systems*, Vol. 50, No. 4, 2005, pp. 195–209. doi:10.1016/j.robot.2004.09.017
[24] Soloviev, A., and Rutkowski, A., "Fusion of Inertial, Optical Flow, and Airspeed Measurements for UAV Navigation in GPS-Denied Environments," *Proceedings of the Defense, Security, and Sensing Conference*, International Soc. for Optics and Photonics Paper 733202, Bellingham, WA, 2009.
[25] Hrabar, S., and Sukhatme, G., "Vision-Based Navigation Through Urban Canyons," *Journal of Field Robotics*, Vol. 26, No. 5, 2009, pp. 431–452. doi:10.1002/rob.v26:5
[26] Sanfourche, M., Delaune, J., Le Besnerais, G., de Plinval, H., Israel, J., Cornic, P., Treil, A., Watanabe, Y., and Plyer, A., "Perception for UAV: Vision-Based Navigation and Environment Modeling," *Aerospace Lab*, No. 4, 2012, pp. 1–19, https://hal.archives-ouvertes.fr/hal-01183691/.
[27] Wu, A., Johnson, E., and Proctor, A., "Vision-Aided Inertial Navigation for Flight Control," *Journal of Aerospace Computing, Information, and Communication*, Vol. 2, No. 9, 2005, pp. 348–360. doi:10.2514/1.16038
[28] Zhang, J., Wu, Y., Liu, W., and Chen, X., "Novel Approach to Position and Orientation Estimation in Vision-Based UAV Navigation," *IEEE Transactions on Aerospace and Electronic Systems*, Vol. 46, No. 2, 2010, pp. 687–700. doi:10.1109/TAES.2010.5461649
[29] Hwangbo, M., and Kanade, T., "Visual-Inertial UAV Attitude Estimation Using Urban Scene Regularities," *Proceedings of the International Conference on Robotics and Automation*, IEEE Publ., Piscataway, NJ, 2011, pp. 2451–2458.
[30] Wang, T., Wang, C., Liang, J., Chen, Y., and Zhang, Y., "Vision-Aided Inertial Navigation for Small Unmanned Aerial Vehicles in GPS-Denied Environments," *International Journal of Advanced Robotic Systems*, Vol. 10, No. 276, 2013, http://www.intechopen.com/journals/international_journal_of_advanced_robotic_systems/vision-aided-inertial-navigation-for-small-unmanned-aerial-vehicles-in-gps-denied-environments. doi:10.5772/56660
[31] Shim, D., Chung, H., and Sastry, S., "Conflict-Free Navigation in Unknown Urban Environments," *IEEE Robotics and Automation Magazine*, Vol. 13, No. 3, 2006, pp. 27–33. doi:10.1109/MRA.2006.1678136
[32] Soloviev, A., "Tight Coupling of GPS and INS for Urban Navigation," *IEEE Transactions on Aerospace and Electronic Systems*, Vol. 46, No. 4, 2010, pp. 1731–1746. doi:10.1109/TAES.2010.5595591
[33] Tomić, T., Schmid, K., Lutz, P., Domel, A., Kassecker, M., Mair, E., Grixa, I., Ruess, F., Suppa, M., and Burschka, D., "Toward a Fully Autonomous UAV: Research Platform for Indoor and Outdoor Urban Search and Rescue," *IEEE Robotics Automation Magazine*, Vol. 19, No. 3, 2012, pp. 46–56. doi:10.1109/MRA.2012.2206473
[34] Euston, M., Coote, P., Mahony, R., Kim, J., and Hamel, T., "A Complementary Filter for Attitude Estimation of a Fixed-Wing UAV," *Proceedings of the International Conference on Intelligent Robots and Systems*, IEEE/RSJ, Nice, France, 2008, pp. 340–345.
[35] Lai, Y., Jan, S., and Hsiao, F., "Development of a Low-Cost Attitude and Heading Reference System Using a Three-Axis Rotating Platform," *Sensors*, Vol. 10, No. 4, 2010, pp. 2472–2491. doi:10.3390/s100402472

[36] Kingston, D. B., and Beard, A., "Real-Time Attitude and Position Estimation for Small UAVs Using Low-Cost Sensors," *3rd "Unmanned Unlimited" Technical Conference, Workshop, and Exhibit*, AIAA Paper 2004-6488, 2004.
[37] de Marina, H., Espinosa, F., and Santos, C., "Adaptive UAV Attitude Estimation Employing Unscented Kalman Filter, FOAM and Low-Cost MEMS Sensors," *Sensors*, Vol. 12, No. 12, 2012, pp. 9566–9585.
doi:10.3390/s120709566
[38] Langelaan, J., Alley, N., and Neidhoefer, J., "Wind Field Estimation for Small Unmanned Aerial Vehicles," *Journal of Guidance, Control, and Dynamics*, Vol. 34, No. 4, 2011, pp. 1016–1030.
doi:10.2514/1.52532
[39] Beard, R., "State Estimation for Micro Air Vehicles," *Innovations in Intelligent Machines-1*, Springer, New York, 2007, pp. 173–199.
[40] Dorobantu, A., Murch, A., Mettler, B., and Balas, G., "System Identification for Small, Low-Cost, Fixed-Wing Unmanned Aircraft," *Journal of Aircraft*, Vol. 50, No. 4, 2013, pp. 1117–1130.
doi:10.2514/1.C032065
[41] "3DM-GX3-25 Miniature Attitude Heading Reference System," *LORD MicroStrain Sensing Systems*, Willston, VT, 2013, http://files.microstrain.com/3DM-GX3-25-Attitude-Heading-Reference-System-Data-Sheet.pdf [accessed 27 December 2015].
[42] "GPS: Essentials of Satellite Navigation," Compendium GPS-X-02007-D, 2009, https://www.u-blox.com/en/technology/GPS-X-02007.pdf.
[43] Beard, R., and McLain, T., *Small Unmanned Aircraft*, Princeton Univ. Press, Princeton, NJ, 2012.
[44] Nemra, A., and Aouf, N., "Robust INS/GPS Sensor Fusion for UAV Localization Using SDRE Nonlinear Filtering," *IEEE Sensors Journal*, Vol. 10, No. 4, 2010, pp. 789–798.
doi:10.1109/JSEN.2009.2034730
[45] Rhudy, M. B., Gu, Y., and Napolitano, M., "Low-Cost Loosely-Coupled Dual GPS/INS for Attitude Estimation with Application to a Small UAV," *Guidance, Navigation, and Control and Co-Located Conferences*, AIAA Paper 2013-4957, 2013.
[46] MacGougan, G., Lachapelle, G., Klukas, R., Siu, K., Garin, L., Shewfelt, J., and Cox, G., "Degraded GPS Signal Measurements with a Stand-Alone High Sensitivity Receiver," *Proceedings of the National Technical Meeting*, Vol. 28, ION, San Diego, CA, 2002, p. 191–204, https://www.ion.org/publications/abstract.cfm?jp=p&articleID=209.
[47] Modsching, M., Kramer, R., and ten Hagen, K., "Field Trial on GPS Accuracy in a Medium Size City: The Influence of Built-Up," *Proceedings of the 3rd Workshop on Positioning, Navigation and Communication*, Hannover, Germany, 2006, pp. 209–218, http://wpnc.net/fileadmin/WPNC06/Proceedings/30_Field_trial_on_GPS_Accuracy_in_a_medium_size_city_The_influence_of_builtup.pdf.
[48] Horn, B., and Schunck, B., "Determining Optical Flow," *Artificial Intelligence*, Vol. 17, No. 1, 1981, pp. 185–203.
doi:10.1016/0004-3702(81)90024-2
[49] Srinivasan, M., Lehrer, M., Kirchner, W., and Zhang, S., "Range Perception Through Apparent Image Speed in Freely Flying Honeybees," *Visual Neuroscience*, Vol. 6, No. 5, 1991, pp. 519–535.
doi:10.1017/S095252380000136X
[50] Serres, J., Ruffier, F., Viollet, S., and Franceschini, N., "Toward Optic Flow Regulation for Wall-Following and Centring Behaviours," *International Journal of Advanced Robotic Systems*, Vol. 3, No. 2, 2006, pp. 147–154.
[51] Hrabar, S., and Sukhatme, G., "A Comparison of Two Camera Configurations for Optic-Flow Based Navigation of a UAV Through Urban Canyons," *Proceedings of the International Conference on Intelligent Robots and Systems*, Vol. 3, IEEE/RSJ, Sendai, PRC, 2004, pp. 2673–2680.
[52] Hrabar, S., and Sukhatme, G., "Optimum Camera Angle for Optic Flow-Based Centering Response," *Proceedings of the International Conference on Intelligent Robots and Systems*, IEEE/RSJ, Beijing, 2006, pp. 3922–3927.
[53] Beard, R. W., Kingston, D., Quigley, M., Snyder, D., Christiansen, R., Johnson, W., McLain, T., and Goodrich, M., "Autonomous Vehicle Technologies for Small Fixed-Wing UAVs," *Journal of Aerospace Computing, Information, and Communication*, Vol. 2, No. 1, 2005, pp. 92–108.
doi:10.2514/1.8371
[54] "Air Data Systems Data Sheet," Aeroprobe Corp., Christiansburg, VA, 2014.
[55] Yeo, D., Henderson, J., and Atkins, E., "An Aerodynamic Data System for Small Hovering Fixed-Wing UAS," *Proceedings of the Guidance, Navigation, and Control Conference*, AIAA Paper 2009-5756, 2009.
[56] Quigley, M., Barber, B., Griffiths, S., and Goodrich, M., "Towards Real-World Searching with Fixed-Wing Mini-UAVs," *Proceedings of the International Conference on Intelligent Robots and Systems*, Vol. 6543, IEEE/RSJ, Edmonton, AB, Canada, 2005, pp. 3028–3033.
[57] Jung, D., and Tsiotras, P., "Inertial Attitude and Position Reference System Development for a Small UAV," *AIAA Infotech@Aerospace 2007 Conference and Exhibit*, AIAA Paper 2007-2763, 2007.
[58] Wang, S., Min, J., and Yi, B., "Location Based Services for Mobiles: Technologies and Standards," *Proceedings of the International Conference on Communication*, IEEE Publ., Piscataway, NJ, 2008, pp. 35–38.
[59] "Wireless E911 Location Accuracy Requirements," Federal Communications Commission, *PS Docket 07–114, Second Report and Order*, 2010.
[60] Kürner, T., "Requirements for X-Map-Estimation In Wireless Self-Organizing Networks," FP7 ICT-SOCRATES, Brunswick, Germany, 2009, http://www.fp7-socrates.eu/index.html@q=node%252F10.html.
[61] Neuland, M., Kurner, T., and Amirijoo, M., "Influence of Positioning Error on X-Map Estimation in LTE," *Proceedings of the 73rd Vehicular Technology Conference*, IEEE Publ., Piscataway, NJ, 2011, pp. 1–5.
[62] Ericsson, "Positioning with LTE," White Paper, 2011, http://www.sharetechnote.com/Docs/WP-LTE-positioning.pdf.
[63] "LTE; Evolved Universal Terrestrial Radio Access (E-UTRA); Requirements for Support of Assisted Global Navigation Satellite System (A-GNSS) (3GPP TS 36.171 version 9.1.0 Release 9)," *Technical Specification Group Radio Access Network*, 3GPP, http://www.etsi.org/deliver/etsi_ts/136100_136199/136171/09.01.00_60/ts_136171v090100p.pdf.
[64] Ficek, M., Pop, T., and Kencl, L., "Active Tracking in Mobile Networks: An In-Depth View," *Computer Networks*, Vol. 57, No. 9, 2013, pp. 1936–1954.
doi:10.1016/j.comnet.2013.03.013
[65] Kyung-Hoon, W., "An Enhanced Observed Time Difference of Arrival Based Positioning Method for 3GPP LTE System," *IEICE Transactions on Communications*, Vol. 95, No. 3, 2012, pp. 961–971.
[66] Bull, J. F., "Wireless Geolocation," *IEEE Vehicular Technology Magazine*, Vol. 4, No. 4, 2009, pp. 45–53.
doi:10.1109/MVT.2009.934669
[67] Ranta-aho, K., "Performance of 3GPP Rel-9 LTE Positioning Methods," *Proceedings of the 2nd Invitational Workshop on Opportunistic RF Localization for Next Generation Wireless Devices*, Slides, 2010.
[68] Levinson, J., Montemerlo, M., and Thrun, S., "Map-Based Precision Vehicle Localization in Urban Environments," *Proceedings of Robotics: Science and Systems III*, Georgia Institute of Technology, Atlanta, GA, 2007.
[69] Culhane, A. A., "Development of an Obstacle Detection System for Human Supervisory Control of a UAV in Urban Environments," Ph.D. Thesis, Virginia Polytechnic Inst. and State Univ., Blacksburg, VA, 2007.
[70] "Scanning Laser Range Finder UTM-30LX-EW Specification Sheet," Hokuyo Automatic Co., Ltd., Osaka, Japan, 2012.
[71] "BYTES of the BIG APPLE," *Dept. of City Planning*, New York, http://www.nyc.gov/html/dcp/html/bytes/applbyte.shtml [accessed 27 December 2015].
[72] Ducard, G., "Fault-Tolerant Flight Control and Guidance Systems: Practical Methods for Small Unmanned Aerial Vehicles," *Advances in Industrial Control*, Springer, New York, 2009, https://www.springer.com/series/1412.
[73] Burl, J., *Linear Optimal Control: H_2 and H_∞ Methods*, 1st ed., Addison-Wesley, Boston, MA, 1998.
[74] Groves, P., "Shadow Matching: A New GNSS Positioning Technique for Urban Canyons," *Journal of Navigation*, Vol. 64, No. 3, July 2011, pp. 417–430.
doi:10.1017/S0373463311000087

[75] Ristic, B., Arulampalm, S., and Gordon, N., *Beyond the Kalman Filter: Particle Filters for Tracking Applications*, Artech House, Inc., Norwood, MA, 2004.
[76] Kalman, R., "A New Approach to Linear Filtering and Prediction Problems," *Journal of Basic Engineering*, Vol. 82, Series D, 1960, pp. 35–45.
[77] Welch, G., and Bishop, G., "An Introduction to Kalman Filtering," Dept. of Computer Science and Engineering, Univ. of North Carolina at Chapel Hill, TR, Chapel Hill, NC, 2001, http://www.cs.unc.edu/~tracker/media/pdf/SIGGRAPH2001_CoursePack_08.pdf.
[78] Gordon, N., Salmond, D., and Smith, A., "Novel Approach to Nonlinear/Non-Gaussian Bayesian State Estimation," *IEEE Proceedings F: Radar and Signal Processing*, Vol. 140, No. 2, 1993, pp. 107–113.
doi:10.1049/ip-f-2.1993.0015
[79] Evensen, G., "Sequential Data Assimilation with a Nonlinear Quasi-Geostrophic Model Using Monte Carlo Methods to Forecast Error Statistics," *Journal of Geophysical Research: Oceans (1978–2012)*, Vol. 99, No. C5, 1994, pp. 10143–10162.
[80] Gillijns, S., Mendoza, O., Chandrasekar, J., De Moor, B., Bernstein, D., and Ridley, A., "What is the Ensemble Kalman Filter and How Well Does It Work?" *Proceedings of the American Control Conference*, Minneapolis, MN, 2006, pp. 4448–4453, http://ieeexplore.ieee.org/xpl/login.jsp?tp=&arnumber=1657419&url=http%3A%2F%2Fieeexplore.ieee.org%2Fxpls%2Fabs_all.jsp%3Farnumber%3D1657419.
[81] Roumeliotis, S., and Burdick, J., "Stochastic Cloning: A Generalized Framework for Processing Relative State Measurements," *Proceedings of the International Conference on Robotics and Automation*, IEEE Publ., Piscataway, NJ, 2002, pp. 1788–1795.
[82] Eustice, R., Singh, H., and Leonard, J., "Exactly Sparse Delayed-State Filters for View-Based SLAM," *IEEE Transactions on Robotics*, Vol. 22, No. 6, 2006, pp. 1100–1114.
doi:10.1109/TRO.2006.886264
[83] Bartels, C., and De Haan, G., "Smoothness Constraints in Recursive Search Motion Estimation for Picture Rate Conversion," *IEEE Transactions on Circuits and Systems for Video Technology*, Vol. 20, No. 10, 2010, pp. 1310–1319.
doi:10.1109/TCSVT.2010.2058474
[84] Baker, S., Scharstein, D., Lewis, J., Roth, S., Black, M., and Szeliski, R., "A Database and Evaluation Methodology for Optical Flow," *International Journal of Computer Vision*, Vol. 92, No. 1, 2011, pp. 1–31.
doi:10.1007/s11263-010-0390-2
[85] Amirjoo, M., Jorgueseski, L., Kurner, T., Litjens, R., Neuland, M., Scmelz, L., and Turke, U., "Cell Outage Management in LTE Networks (COST 2100 TD (09) 941)," FP7-ICT-SOCRATES, Slides, 2009, http://www.fp7-socrates.eu/index.html@q=node%252F10.html.
[86] Lopes, H., Kampen, E., and Chu, Q., "Attitude Determination of Highly Dynamic Fixed-Wing UAVs with GPS/MEMS-AHRS Integration," *Guidance, Navigation, and Control and Co-Located Conferences*, AIAA Paper 2012-4460, 2012.
[87] Langelaan, J., Spletzer, J., Montella, C., and Grenestedt, J., "Wind Field Estimation for Autonomous Dynamic Soaring," *International Conference on Robotics and Automation*, IEEE Publ., Piscataway, NJ, 2012, pp. 16–22.
[88] "Micro Air Data System User Manual," Aeroprobe Corp., Christiansburg, VA, 2013.
[89] Ramprasadh, C., and Arya, H., "Estimation of Aerodynamic Angles in a Mini Aerial Vehicle Under Turbulent Atmosphere," *Atmospheric Flight Mechanics Conference*, AIAA Paper 2011-6517, 2011.

G. Chowdhary
Associate Editor